Radio-frequency sheath-plasma interactions with magnetic field tangency points along the sheath surface

H. Kohno[1,a)], J. R. Myra[2], and D. A. D'Ippolito[2]

[1]*Department of Physics, Lehigh University, 16 Memorial Drive East, Bethlehem, PA 18015, USA*

[2]*Lodestar Research Corporation, 2400 Central Avenue P-5, Boulder, CO 80301, USA*

[a)] Electronic mail: kohno@mse.kyutech.ac.jp (The present affiliation of the corresponding author is as follows: Department of Mechanical Information Science and Technology, Kyushu Institute of Technology, 680-4 Kawazu, Iizuka, Fukuoka 820-8502, Japan.)

Abstract

Computer simulations of radio-frequency (RF) waves propagating across a two-dimensional (2D) magnetic field into a conducting boundary are described. The boundary condition for the RF fields at the metal surface leads to the formation of an RF sheath, which has previously been studied in one-dimensional models. In this 2D study, it is found that rapid variation of conditions along the sheath surface promote coupling of the incident RF branch (either fast or slow wave) to a short-scale-length sheath plasma wave (SPW). The SPW propagates along the sheath surface in a particular direction dictated by the orientation of the magnetic field with respect to the surface, and the wave energy in the SPW accumulates near places where the background magnetic field is tangent to the surface.

PACS: 52.35.Mw, 52.40.Kh, 52.50.Qt, 52.55.Fa

I. INTRODUCTION

Radio-frequency (RF) waves in the ion cyclotron range of frequencies (ICRF) are commonly used to heat the plasma and drive currents in tokamak experiments. While many successes have been achieved with the application of ICRF auxiliary power, it has been known for some time [1] that undesirable interactions of high power waves with the plasma boundary and material surfaces can sometimes occur. A prime candidate for explaining these interactions is the mechanism of RF-driven sheaths [1-8] which have been shown in experiments and modeling studies [9-31] to describe qualitatively, and sometimes quantitatively the observations of enhanced plasmas potentials, local surface heating, enhanced impurity sputtering and loss of RF power in the boundary. Both RF interactions with the launching structure and so-called far-field sheath interactions [32,33] with more distant surfaces are of interest.

Early theoretical work and modeling calculated RF-driven sheath potentials and assessed their consequences assuming the RF wave fields were given. In practice, these fields were taken from wave-solvers which did not incorporate sheath physics, and in the case of antenna modeling, for wave solvers which used vacuum rather than plasma in the volume immediately surrounding the antenna structure. More recently, there has been an effort to calculate the RF fields self-consistently in the presence of RF sheaths. Because sheaths occur

on the scale of the Debye length, which is much smaller than domain sizes or RF wavelengths of interest for fusion applications, approximate RF sheath boundary condition approaches have been developed [34-38]. These approaches effectively treat the sheath as a thin vacuum layer, and thus capture the important effect of sheath capacitance on the boundary. In principle, this kind of approach should permit a wide variety of interesting RF-surface interactions to be modeled with greater realism than has been possible up until now.

In the present paper, we take a step in that direction, building upon previous work [37] in which a new code, rfSOL [38], was employed to study aspects of self-consistent wave propagation and sheath interaction in a two-dimensional (2D) slab geometry. Various phenomena seen in simpler analytical models [34,39-42] such as multiple roots, hysteresis effects, and the presence and characteristics of the sheath-plasma waves [43-46], were studied numerically in the presence of spatially varying plasma density and background magnetic field.

Like the previous work, the present study also employs 2D geometry in a rectangular domain. However, here, one seemingly innocuous new feature is introduced which turns out to have profound physical implications: we allow variation along the sheath surface such that the background magnetic field can be tangent to the surface at one or more points. These tangency or near-tangency interactions are the focus of our paper. We will show that they play

an important role in governing the distribution of wave energy and induced potentials along the sheath surface, and thus are of paramount importance for understanding the nature of RF wave interactions with surfaces in more realistic geometries. More generally, we will show that rapid variation of conditions (in particular, the background magnetic field to surface contact angle) along the sheath boundary promotes strong RF-sheath interactions.

In passing, we note that the rapid variation of this contact angle at the main limiter was invoked to explain the experimental observation of large ($>100\,\mathrm{V}$) plasma potentials far from the antenna in Alcator C-Mod [47]. This conclusion was reached using a one-dimensional (1D) model [48]. The present 2D treatment of a conceptually-related problem is an important step forward towards realistic modeling.

The plan of our paper is as follows. In Sec. II we briefly summarize the basic model for sheath-plasma interactions and provide references to underlying work. The numerical model is described in Sec. III, with results for evanescent slow wave (SW) interactions presented in Sec. III A and propagating fast wave (FW) sheath interactions presented in Sec. III B. Our conclusions are given in Sec. IV. Details of an analytical model for sheath-plasma wave (SPW) propagation along the surface are given in the Appendix.

II. MODEL FOR SHEATH-PLASMA INTERACTIONS

In this section, we briefly summarize the equations that govern the behavior of plasma waves in the scrape-off layer (SOL) and the interaction between the ICRF waves and the sheaths on metal surfaces. Since the details are described in our previous papers [37,38], we will not repeat all of them here. In the following analysis, we assume that only deuterium is considered as an ion species; however, the formalism is easily generalized to different or multiple species by appropriate modifications to the dielectric tensor.

The governing equation for plasma waves in the SOL is a combined form of Maxwell's equations described as

$$\nabla \times \nabla \times \mathbf{E} - \frac{\omega^2}{c^2} \boldsymbol{\varepsilon} \cdot \mathbf{E} - i\omega\mu_0 \mathbf{J}_{\text{ext}} = \mathbf{0}, \tag{1}$$

where the electric field $\mathbf{E}$ and the external current $\mathbf{J}_{\text{ext}}$ vary on the RF time scale. Here, ω is the applied ICRF wave frequency, c is the speed of light, and μ_0 is the permeability in vacuum. The dielectric tensor $\boldsymbol{\varepsilon}$ is given based on the cold plasma model [49]. At the metal wall, the sheath effect is taken into account by means of a sheath boundary condition (sheath BC), which is written as follows:

$$\mathbf{E}_{\text{t}} = \nabla_{\text{t}} \left(\frac{\Delta_{\text{sh}}}{\varepsilon_{\text{sh}}} D_{\text{n}} \right). \tag{2}$$

Here, Δ_{sh} is the time-averaged sheath width, ε_{sh} is the dielectric constant in the sheath (in this study we assume that $\varepsilon_{\text{sh}} = \varepsilon_0$, where ε_0 is the dielectric constant in vacuum),

$D_{\mathrm{n}}\left(=\varepsilon_0 \mathbf{s}\cdot\boldsymbol{\varepsilon}\cdot\mathbf{E}\right)$ is the component of the electric displacement normal to the sheath (and $\mathbf{s}$ is the unit normal vector pointing into the plasma), and the subscript t denotes the two components tangential to the boundary. We recall that the sheath BC depends on scale separation, i.e., the Debye length and the sheath width must be the smallest spatial scales in the problem. In particular, at very low densities where the sheath width becomes large, the boundary condition may no longer be valid. Also, the sheath BC tends to be significant only when $\varepsilon_{||} >> 1$; otherwise, the right-hand side of Eq. (2) is negligible. In a manner consistent with the Child-Langmuir law [50,51], the sheath width is written as follows:

$$\Delta_{\mathrm{sh}} = \left(\frac{eC_{\mathrm{sh}}}{\varepsilon_{\mathrm{sh}} T_{\mathrm{e}}} \left| D_{\mathrm{n}} \right| \right)^3 \lambda_{\mathrm{De}}^4 + C_{\mathrm{th}} \lambda_{\mathrm{De}}, \tag{3}$$

where e is the electric charge, C_{sh} is an order-unity constant relating the rectified and RF potentials (which is fixed at 0.6 in this study), T_{e} is the electron temperature, and λ_{De} is the electron Debye length defined as $\lambda_{\mathrm{De}} = \left(\varepsilon_0 T_{\mathrm{e}} / n_{\mathrm{e}} e^2\right)^{1/2}$ with n_{e} the equilibrium electron density. The first and second terms on the right hand side of Eq. (3) are the RF and thermal sheath contributions to the self-consistent sheath width, respectively. The coefficient C_{th} has different forms depending on whether the magnetic field angle is smaller (ion poor sheath) or larger (electron poor sheath) than a critical value. Using a polynomial fit to transition smoothly between the two limits, C_{th} is given by

$$C_{\text{th}} = \begin{cases} a_1 |b_{\text{n}}|^4 + a_2 |b_{\text{n}}|^3 & \text{for } |b_{\text{n}}| \le b_{\text{crit}} \\ \left\{ \ln\left[\left(\frac{m_{\text{i}}}{m_{\text{e}}} \right)^{1/2} |b_{\text{n}}| \right] \right\}^{3/4} & \text{for } |b_{\text{n}}| > b_{\text{crit}}, \end{cases} \tag{4}$$

where m_{i} and m_{e} are the ion mass and electron mass, respectively, and b_{n} is defined by $b_{\text{n}} = B_{0\text{n}} / |\mathbf{B}_0|$ (a component of $\mathbf{b} = \mathbf{B}_0 / |\mathbf{B}_0|$) where $\mathbf{B}_0$ is the background magnetic field and $B_{0\text{n}}$ is its component normal to the sheath. The coefficients a_1 and a_2 are determined so as to satisfy the continuity of C_{th} and $dC_{\text{th}} / d|b_{\text{n}}|$ at $|b_{\text{n}}| = b_{\text{crit}}$, where $b_{\text{crit}} \approx (m_{\text{e}} / m_{\text{i}})^{1/2}$. The continuity in the derivative of C_{th} is especially important when the background magnetic field varies along the sheath surface and includes $B_{0\text{n}} = 0$ on the sheath; otherwise, the electric field component tangential to the sheath surface becomes discontinuous near the flux-surface tangency point(s) according to Eq. (2). In this study, as mentioned above, we assume a deuterium plasma and the value of b_{crit} is fixed at 0.02.

The combined form of Maxwell's equations and the sheath BC are self-consistently solved with the rfSOL code, which is based on a finite element method as presented in Ref. [38]. The calculations are performed on the Hopper Cray XE6 computer system at the National Energy Research Scientific Computing Center (NERSC).

III. NUMERICAL SIMULATION OF SHEATH-PLASMA INTERACTIONS

In our previous work, we have mainly analyzed 2D sheath-plasma interaction problems for spatially constant background magnetic fields [37,38]. In the present numerical analysis, we consider solutions of the sheath-plasma interactions for spatially varying background magnetic fields whose flux surfaces have tangency points at a boundary. This magnetic field configuration actually happens with limiter surfaces in a tokamak.

Figure 1 shows the problem definition which corresponds to some extent to a simplified geometry of the edge plasma region including an antenna in the poloidal cross-section of a tokamak. The origin in the Cartesian coordinate system is placed at the bottom-left corner of the domain. The electric field is solved subject to the sheath BC on the right-hand side, the conducting-wall boundary condition (conducting-wall BC) on the left-hand side, and a periodic boundary condition that connects the top and bottom of the domain. The antenna surface current is given by a sine function in the y direction as follows:

$$\mathbf{J}_{\text{ext}} = K(y)\delta(x - D_{\text{lw-ant}})\mathrm{e}^{i(k_z z - \omega t)}\mathbf{e}_y, \tag{5}$$

with

$$K(y) = K_{\max}\cos^2\left(\frac{\pi\,\hat{y}}{L_{\text{ant}}}\right), \tag{6}$$

where $\hat{y} = y - L_y/2$. Thus, the antenna current is maximum at the center of the antenna ($\hat{y} = 0$) and is zero at the two ends. In Eq. (5), k_z is the toroidal wavenumber component,

$\mathbf{e}_y$ is the unit vector in the y direction (the same shall apply to $\mathbf{e}_x$ and $\mathbf{e}_z$), and $K_{\max}$ is the maximum antenna current density. The spatially varying background magnetic field is given by

$$\mathbf{B}_0 = B_{0z}\mathbf{e}_z + \mathbf{e}_z \times \nabla \Psi_{\mathrm{p}}, \tag{7}$$

where

$$\Psi_{\mathrm{p}} = -B_{\mathrm{p}} x\left\{A + \cos\left[k_{\mathrm{p}}\left(y - y_{\mathrm{p}}\right) + \Theta\right]\right\}. \tag{8}$$

where B_{p}, A, k_{p}, y_{p}, and Θ are specified parameters. It can be easily checked that the above expression, together with constant B_{0z}, satisfies $\nabla \cdot \mathbf{B}_0 = 0$. The model magnetic field of Eq. (8) is not meant to map literally to tokamak geometry, but is intended only to enable conceptual points to be addressed in the present paper - in particular as will be evident from Fig. 2, this model allows two tangency points of the field with the wall.

All the calculations in this study will be conducted with a linear sheath BC, in which the electric field contribution to the sheath width (i.e., the first term of Eq. (3)) is omitted. However, it is important to mention that the sheath width varies along the sheath surface (i.e., $\Delta_{\mathrm{sh}} = \Delta_{\mathrm{sh}}(y)$) due to the definition of C_{th} (see Eq. (4)) in conjunction with the spatially varying background magnetic field given in Eq. (7). We will show that this variation controls the strength of the interaction of waves with the sheath and the propagation of SPWs.

A. Evanescent plasma wave-sheath interactions

We consider first the sheath-plasma interactions for evanescent waves and investigate the role of flux-surface tangency points at a boundary. Based on Fig. 1, the calculation domain, antenna length, and its position are determined such that $L_x = 0.4\,\mathrm{m}$, $L_y = 0.8\,\mathrm{m}$, $L_{\mathrm{ant}} = 0.05\,\mathrm{m}$, and $D_{\mathrm{lw\text{-}ant}} = 0.2\,\mathrm{m}$. The quasi-neutral plasma density is fixed at $n_{\mathrm{i}} = n_{\mathrm{e}} = 2\times10^{18}\ \mathrm{m}^{-3}$ over the whole domain, and the background magnetic field parameters in Ψ_{p} are $B_{\mathrm{p}} = 0.4\,\mathrm{T}$, $k_{\mathrm{p}} = 2\pi/L_y$, $y_{\mathrm{p}} = L_y/2$, $\Theta = \pi/4$, and $A = 2$. In addition, the toroidal wavenumber component, k_z, is fixed at 10.8 m^{-1}, the electron temperature is 10 eV, the applied frequency is 80 MHz, the toroidal background magnetic field component, B_{0z}, is 4 T, and the maximum antenna current density is 1 A/m. Unless otherwise noted, these values are used as default ones in this and subsequent analyses. The calculation domain is divided by a nonuniform mesh which includes 961×1601 grid points (480×800 nine-node elements) in total; 160×800 nine-node elements in $0 \le x \le D_{\mathrm{lw-ant}}$ and 320×800 elements in $D_{\mathrm{lw-ant}} \le x \le L_x$ are used in the x and y directions, respectively. The grid points in the x direction are concentrated in the vicinity of the sheath in order to accurately resolve the thin layer, within which SPWs exponentially decay, near the flux-surface tangency points at the sheath.

Figure 2 shows the filled contour plot of $\sinh^{-1}\left[\alpha_{\mathrm{amp}}\,\mathrm{Re}\left(E_{\parallel}\right)\right]$, where $E_{\parallel}$ is the electric

field component parallel to the magnetic field line ($E_{\parallel} = \mathbf{E} \cdot \mathbf{B}_0 / |\mathbf{B}_0|$) and α_{amp} is the amplification factor ($\alpha_{\text{amp}} = 1000$) for adjusting colors. The palette colors are chosen to accentuate the smaller fields near the sheath boundary without saturating the fields near the antenna. Here, the antenna and magnetic field lines are also superimposed on the plot. Since this is a plot of $E_{\parallel}$, the FW contribution is considered to be negligible. It is observed that the SW propagates along the magnetic field lines although it is evanescent from the antenna position. In addition, the SPW is generated on the sheath surface between the "convex" flux-surface tangency point ($y = 0.3\,\text{m}$) and the intersection point ($y = 0.6\,\text{m}$) of a magnetic field line penetrating the antenna and the wall (hereafter, the flux-surface tangency points ($b_{\text{n}} = 0$) from which the magnetic field lines inside the plasma are seen as convex and concave curves are simply called the convex and concave tangency points at the sheath surface, respectively). While the present geometry is too simple to apply directly to a tokamak, in general the complex magnetic fields of shaped diverted plasmas, and realistic vessel walls can exhibit both types (convex and concave) of interactions. This is also confirmed in Fig. 3, which shows the variations of the real part of the parallel electric field component along the sheath surface for two different boundary conditions at the right wall; here, the result obtained by imposing the conducting-wall BC, $\mathbf{E}_{\text{t}} = \mathbf{0}$, is added for comparison. It is seen that the SPW is generated only by imposing the sheath BC. Furthermore, it is important to notice that

the SPW is driven in the narrow region within which the magnetic field lines connect the antenna to the wall and accumulation of its energy occurs at the convex tangency point. (This in spite of the fact that the concave point is closer to where the field lines strike the wall. In this regard we find that the placement of the antenna influences the field strength and pattern, but not the tendency for SPW accumulation at the convex point.) The next part of this section will be devoted to clarify the mechanism of this phenomenon.

B. Electromagnetic SW-SPW dispersion relation

The physics involved in Fig. 2 or 3 can be uncovered by using the following two equations, which are derived in Appendix:

$$n_{\perp}^2 \varepsilon_{\perp} + n_{\parallel}^2 \varepsilon_{\parallel} = \varepsilon_{\perp} \varepsilon_{\parallel}, \tag{9}$$

$$n_{\mathrm{t}}^2 k_{\parallel} - \varepsilon_{\perp} \mathbf{k}_{\mathrm{t}} \cdot \mathbf{b}_{\mathrm{t}} = i k_{\mathrm{t}}^2 \Delta_{\mathrm{sh}} b_{\mathrm{n}} \varepsilon_{\parallel} \left(n_{\parallel}^2 - \varepsilon_{\perp} \right), \tag{10}$$

where $n_{\perp}$ and $n_{\parallel}$ are the components of the index of refraction, which is defined as $\mathbf{n} = c\mathbf{k}/\omega$, perpendicular and parallel to $\mathbf{B}_0$, respectively; $\varepsilon_{\perp}$, $\varepsilon_{\parallel}$ are the components of $\boldsymbol{\varepsilon}$ (see Ref. [37] for the definitions); $k_{\mathrm{t}}^2 = \mathbf{k}_{\mathrm{t}} \cdot \mathbf{k}_{\mathrm{t}}$ (or $n_{\mathrm{t}}^2 = \mathbf{n}_{\mathrm{t}} \cdot \mathbf{n}_{\mathrm{t}}$) where $\mathbf{k}_{\mathrm{t}}$ comes from the conversion $\nabla \to i\mathbf{k}_{\mathrm{t}}$.

As discussed in the Appendix, Eq. (9) is the local EM (electromagnetic) SW dispersion relation in the volume, and Eq. (10) is the appropriate boundary condition at the

sheath surface. We solve the two equations simultaneously for complex k_x and k_y with ω, k_z, and local values for the plasma parameters given as described above. Also, note that the sheath width is calculated using Eqs. (3) and (4) (here, the first term in Eq. (3) is neglected). The unit normal to the sheath (pointing into the plasma) is in the $-\mathbf{e}_x$ direction (i.e., $\mathbf{s}=-\mathbf{e}_x$) according to Fig. 1. The profiles of B_{0x} and B_{0y} are shown in Fig. 4(a). Note the tangency points where $B_{0x}=0$.

Taking $y=0.4\,\mathrm{m}$ on the sheath as a representative point, eight modes are obtained from Eqs. (9) and (10). Five of the modes among them satisfy $\mathrm{Im}(k_x)<0$ and are therefore physically acceptable because they evanesce into the plasma, since our phase convention is $\sim\exp(i\mathbf{k}\cdot\mathbf{x}-i\omega t)$. Further, two modes have $\mathrm{Re}(k_y)\sim 200$ to 300 m^{-1} and therefore have short wavelengths on the order of what we observe in Fig. 3. They are weakly evanescent in y, and they also satisfy the SW ordering ($n_\perp^2\sim\varepsilon_\parallel$). We concentrate on them in the following.

The profile of k_y along the sheath surface is shown in Fig. 4(b). Solutions are ill-posed and therefore suppressed in a narrow band near the points where $B_{0x}=0$. This profile is one important ingredient in understanding the physical behavior of the roots. Below the convex point ($y<0.3\,\mathrm{m}$) both modes decay with increasing y (i.e., $\mathrm{Im}(k_y)>0$), while above the convex point they both grow. Opposite behavior occurs near the concave point ($y=0.7\,\mathrm{m}$).

The second key ingredient in understanding the physical behavior of the roots is the real part of the group velocity v_{gy} shown in Fig. 4(c). Below the convex point ($y < 0.3\,\mathrm{m}$) the wave energy propagates in the direction of increasing y, i.e., towards the convex point, for the red mode (i.e., the mode with direction marked with the thick red arrows), and away from the convex point for the blue mode (thin blue arrows). Similar arguments can be made for the other regions.

Finally, we combine the information about the direction of exponential decay with the information about the direction of propagation. The results can be summarized quite simply: the red mode (plotted with thick lines) decays in the direction of energy propagation (i.e., the direction of v_{gy}) while the blue mode (plotted with thin lines) grows in the direction of energy propagation. Furthermore, it is seen that the convex (concave) point attracts (repels) the red mode while the opposite is true for the blue mode.

We can make a physical argument as to why the red mode should be preferred over the blue one. There is no apparent source of free energy or instability in the physics model of Eqs. (9) and (10), which is local in y on the sheath surface, and therefore does not know about gradients of the background magnetic field. Thus, we *hypothesize* that only the red mode which decays in the direction of energy propagation is physical. It must be admitted that growing modes do in fact happen in physical systems, sometimes with very subtle sources of

free energy. However, in this case we judge a root to be physical not only by considering the analytical theory and stability arguments but also by comparison with numerical results.

Evidently, it is the red (stable) mode that explains the difference of the convex and concave points observed in the numerical result. The red mode propagates energy away from the concave point and towards the convex point. The dramatic slowing of the group velocity near $y = 0.3\,\mathrm{m}$ should lead to an accumulation of wave energy there. Closer to the convex point, the physical mode experiences exponential decay, although the decay is very slow (in fact, $\mathrm{Im}(k_y)$ is more than 10 times smaller than $\mathrm{Re}(k_y)$). Thus, the decay is not evident in the present numerical result.

As a next numerical investigation, the SPW behaviors are compared by slightly increasing the periodic length of the domain (i.e., L_y). Figure 5 shows the variations of the real part of a perpendicular electric field component along the sheath surface for two different lengths of L_y: $L_y = 0.8$ (default) and 0.9 m. Here, the perpendicular component, $E_{\perp y}$, is defined as $E_{\perp y} = (\mathbf{E} - E_{\parallel}\mathbf{b}) \cdot \mathbf{e}_y$. Note that k_p which defines the flux surfaces remains fixed at $k_\mathrm{p} = 2\pi / L_y$. It is observed that the point where the SPW is excited is shifted to a larger y-coordinate value. This corresponds to the fact that the field-line intersection point is shifted with an increase in L_y; from the points of intersection both excited SPWs propagate to their corresponding convex tangency points and wave energy accumulation occurs near those

points. These results clearly demonstrate that the SPW is mainly generated by coupling with a SW that has propagated (with evanescence) along the magnetic field line through the plasma volume to the sheath surface. Although not shown in this paper, it is observed that $E_{\perp y}$ of the SPW in the vicinity of the sheath follows the surface and is skewed along the magnetic field lines, which indicates that the profiles of $\mathrm{Re}\left(E_{\perp y}\right)$ shown in Fig. 5 are associated with SWs. Note that the amplitude of the SPW for $L_y = 0.9\,\mathrm{m}$ is smaller than that for $L_y = 0.8\,\mathrm{m}$ since the length of the magnetic field line connecting the antenna to the wall is longer for the former and thus the SW, which evanesces along that field line, is weaker at the wall (note that the SPW is mainly driven by $E_{\parallel}$ at the intersection point between the field line and the wall). One can observe a similar trend in the profiles of $E_{\parallel}$, although their amplitudes are much smaller than those of $E_{\perp}$.

Figures 6 and 7 are the results showing how B_{p} and k_{p} in the expression of the background magnetic field (see Eqs. (7) and (8)) affect the SPW interactions in the present case. In Fig. 6, the profiles of $\mathrm{Re}\left(E_{\perp y}\right)$ are compared with use of two different values of B_{p} ($B_{\mathrm{p}} = 0.4$ and 2 T); here, the periodic domain length, L_y, is increased to 2.14 m, which is comparable to the circumferential length of the outer wall in the Alcator C-Mod device. On the other hand, in Fig. 7 the profiles of $\mathrm{Re}\left(E_{\perp y}\right)$ are compared using two different values of k_{p} ($k_{\mathrm{p}} = 2\pi/L_y$ and $4\pi/L_y$) with the periodic domain length kept at the default one

($L_y = 0.8\,\mathrm{m}$).

It is important to notice that both B_p and k_p affect the scale length of the variation of the background magnetic field along the sheath surface and this affects the coupling of the SPWs. To be more explicit, from Eq. (8), it is clear that k_p affects the scale length of variation directly. Moreover, B_p affects the scale length through variation of the contact angle $\tan^{-1} b_\mathrm{n}$ where b_n is directly proportional to B_p. A straightforward evaluation of the function $C_\mathrm{th}(y)$ given in Eq. (4) shows that for the most extreme case in Fig. 7, $C_\mathrm{th}(y)$ varies on a scale length of the order of a cm or less. The sheath width is given by $\Delta_\mathrm{sh} = C_\mathrm{th}\lambda_\mathrm{De}$ and it makes a transition from zero sheath width at the tangency point to finite sheath width within a short distance away in y (see Fig. 8; here, the phase shift Θ is set at zero). This variation of Δ_sh implies variation of the boundary condition that is seen by the incident RF waves. Rapid scale variation (comparable to or shorter than the incident wavelength) implies a breakdown of eikonal theory, and promotes strong coupling from the incident branch (here the SW) to the short-scale SPW.

C. Propagating FW-sheath interactions

In this section, we show that the wave-sheath interactions described in Sec. III A (e.g., the coupling of an incoming wave to the SPW, and the special role of magnetic tangency

points) are not purely a SW phenomenon. We examine a case with the same parameters as described in the first paragraph in Sec. III A, except that the spatially constant plasma density is fixed at $n_i = n_e = 1.5 \times 10^{20}$ m^{-3}. The density is high enough that the FW propagates and the SW is highly evanescent (see Fig. 9). Recall that the conducting-wall BC is imposed on the left-hand side of the domain (as shown in Fig. 1) and thus the configuration of the model corresponds to a waveguide rather than a tokamak SOL; however, our model is sufficient to investigate the key mechanism in propagating FW-sheath interactions. For the antenna-wall spacing used here, the $E_{||}$ component shown in Fig. 9(a) is small except at the sheath. Unlike Fig. 2, $E_{||}$ at the sheath does not appear to result from a direct field line connection with the antenna. In fact, we infer that the $E_{||}$ at the sheath is due entirely to the SPW. Note that $E_{\perp y}$ in Fig. 9(b) is much larger, and the corresponding wave propagates across the background magnetic field to the wall. These are the characteristics of the FW.

Figure 10 shows a plot of the real part of the perpendicular electric field component, $\mathrm{Re}\left(E_{\perp y}\right)$, along the sheath surface for this case with an incident propagating fast wave. As in the SW examples in Sec. III A, the incoming wave couples to a short-wavelength mode on the sheath, and this coupling occurs only when the sheath BC is used. The short-wavelength mode disappears when the conducting BC is used. This shows that the sheath capacitance is needed for the existence of the wave, and confirms its identity as a SPW. Finally, note that the

SPW accumulate preferentially at the convex point.

D. Discussion

We have shown that sheaths driven by incident (evanescent) slow waves and propagating fast waves in 2D magnetic field geometry have many similarities. In both cases, there is a spatial localization of the energy along the sheath surface which is influenced by varying geometry along that surface and in particular by the presence of magnetic field tangency points.

Let us consider at a heuristic level why fast and slow waves incident on a sheath generate the SPW. Our basic postulate is that the degree to which the incident waves and the boundary conditions fail to conform is what excites the SPWs. The total wave solution (incident, reflected and sheath plasma wave) must of course satisfy the boundary conditions. If the incident wave has a long scale length and there is rapid variation in the boundary condition along the surface, then short scales length modes must necessarily be generated. To make this more precise, we define a scale length L_{sh} along the sheath surface as the *minimum* of

- the background variation of the sheath width, $\left[d\left(\ln \Delta_{\mathrm{sh}}\right)/dy\right]^{-1}$;
- the wavelength of the waves incident on the boundary, $2\pi/k_y$.

In the case of an incident FW, since the FW wavelength is large, the background variation of the sheath width sets L_{sh}. The second effect may be important for an incident SW which has a short scale length to begin with. In both cases, when $L_{sh} \sim \lambda_{SPW}$ (the wavelength of the SPW), the excitation of the latter is efficient and the result is that large sheath voltages can be obtained.

Since λ_{SPW} is short, the matching condition $L_{sh} \sim \lambda_{SPW}$ is usually only satisfied for FWs near tangency points of the magnetic field where Δ_{sh} varies rapidly (see Fig. 8). As we have seen, (see Fig. 2) direct SW excitation of the SPW may also occur away from the tangency points, but the tangency points can further concentrate the SPW.

IV. CONCLUSIONS

In this paper, we have studied the problem of sheaths created by RF waves incident on a conducting wall for the case of 2D curved magnetic fields with tangency points at the sheath surface. An important element in the model is the propagation of a type of surface wave on the sheath called a “sheath plasma wave” (which is abbreviated as SPW). It was shown that allowing spatial variation along the sheath introduces new effects not obtainable in previous 1D sheath models, such as localized deposition of wave energy at the convex tangency points.

This is expected to be relevant to the formation of localized hot spots on the bounding surfaces, which are commonly observed on powered ICRF antennas, but further work is necessary to establish this point.

The present modeling suggests that the variation of conditions (in particular, the background magnetic field to surface contact angle) along the sheath tends to enhance the RF sheath potential and lead to stronger sheath-plasma interactions. Recent work has explored this effect using a qualitative 1D model in connection with the observed large SOL plasma potentials on Alcator C-Mod [47,48]. The present work underscores the need for an accurate treatment of the geometry of the plasma boundary in order to get quantitative results for RF-plasma interactions.

ACKNOWLEDGMENTS

This work was supported by DOE grant No. DE-FC02-05ER54823 with Lodestar Research Corporation under the Scientific Discovery Through Advanced Computing Initiative (SciDAC). The work of H. Kohno was partially supported by a subcontract between Lodestar Research Corporation and Lehigh University. The research also used resources of the National Energy Research Scientific Computing Center, which is supported by the DOE under

Contract No. DE-AC02-05CH11231.

APPENDIX: EM SPW DISPERSION RELATION IN A TILTED BACKGROUND MAGNETIC FIELD

The SPW dispersion relation in a homogeneous plasma is given by the simultaneous solution of the dispersion relation in the plasma volume and the sheath BC. As we have described in Ref. [37], in the electrostatic (ES) case one can obtain two scalar equations, which allow a unique solution for k_x and k_y (the wavenumber components normal and tangential to the sheath surface, respectively) assuming ω and k_z are specified and equilibrium quantities are known. Here, z is the other direction tangential to the sheath surface, but normal to the simulation plane. The EM SPW problem is fundamentally different. For the EM SW, the dispersion relation is written as

$$n_\perp^2 \varepsilon_\perp + n_\parallel^2 \varepsilon_\parallel = \varepsilon_\perp \varepsilon_\parallel . \tag{A1}$$

The sheath BC is written as Eq. (2) which is a vector equation with two non-trivial components. Consequently, the EM case gives three scalar conditions: a dispersion relation, and the two components of the sheath BC. This indicates that the SPW cannot exist as a true eigenmode of the system in the EM theory; instead, it is observed to be driven in EM

problems even when the FW is the primary mode making contact with the wall. In this sense, we may say that the EM SPW is a quasi-mode (i.e., an oscillation which exists only in the presence of a driving force, but is in some sense close to an eigenmode of the system). To describe it approximately, we rewrite Eq. (2) as the two equivalent conditions

$$\nabla_{\mathrm{t}} \cdot \mathbf{E}_{\mathrm{t}} = \nabla_{\mathrm{t}}^2 \left(\frac{\Delta_{\mathrm{sh}}}{\varepsilon_{\mathrm{sh}}} D_{\mathrm{n}} \right), \tag{A2}$$

$$B_{\mathrm{n}} = 0, \tag{A3}$$

and then retain Eq. (A2) which has the sheath physics, and neglect Eq. (A3). In reality, we assume that Eq. (A3) is ultimately satisfied by including the coupling of the driving mode as described in Ref. [33].

To formulate the EM problem, let us express the electric field as follows:

$$\mathbf{E} = -\nabla\Phi - \frac{\partial \mathbf{A}}{\partial t} \approx -i\mathbf{k}\Phi + i\omega A_{\parallel}\mathbf{b}, \tag{A4}$$

where $\mathbf{A}$ is the vector potential and $A_{\parallel}$ is its component parallel to $\mathbf{B}_0$. Since we focus on the interaction between the SW and the sheath here, the vector potential is approximated to $\mathbf{A} \approx A_{\parallel}\mathbf{b}$. Substituting Eq. (A4) into Maxwell's equation

$$\left(\mathbf{nn} - n^2\mathbf{I} + \boldsymbol{\varepsilon}\right) \cdot \mathbf{E} = \mathbf{0}, \tag{A5}$$

(where $\mathbf{I}$ is the unit tensor) one obtains

$$\boldsymbol{\varepsilon} \cdot \mathbf{n}\Phi - \left(\mathbf{nn} - n^2\mathbf{I} + \boldsymbol{\varepsilon}\right) \cdot \left(cA_{\parallel}\mathbf{b}\right) = \mathbf{0}. \tag{A6}$$

Next, we extract coupled equations for Φ and $A_{\parallel}$ by dotting Eq. (A6) with $\mathbf{n}$ and $\mathbf{b}$ to

obtain

$$\mathbf{n}\cdot\boldsymbol{\varepsilon}\cdot\mathbf{n}\Phi-\mathbf{n}\cdot\boldsymbol{\varepsilon}\cdot\left(cA_{\parallel}\mathbf{b}\right)=0, \tag{A7}$$

$$\mathbf{b}\cdot\boldsymbol{\varepsilon}\cdot\mathbf{n}\Phi-\left(-n_{\perp}^{2}+\mathbf{b}\cdot\boldsymbol{\varepsilon}\cdot\mathbf{b}\right)cA_{\parallel}=0. \tag{A8}$$

Substituting the expression for the dielectric tensor

$$\boldsymbol{\varepsilon}=\left(\mathbf{I}-\mathbf{bb}\right)\varepsilon_{\perp}+\mathbf{bb}\varepsilon_{\parallel}+i\mathbf{b}\times\mathbf{I}\varepsilon_{\times} \tag{A9}$$

into Eqs. (A7) and (A8), one gets

$$\left(n_{\perp}^{2}\varepsilon_{\perp}+n_{\parallel}^{2}\varepsilon_{\parallel}\right)\Phi-cn_{\parallel}\varepsilon_{\parallel}A_{\parallel}=0, \tag{A10}$$

$$n_{\parallel}\varepsilon_{\parallel}\Phi-c\left(\varepsilon_{\parallel}-n_{\perp}^{2}\right)A_{\parallel}=0. \tag{A11}$$

A short calculation verifies that Eqs. (A10) and (A11) recover the SW dispersion relation given in Eq. (A1).

Now, look at the sheath BC in Eq. (A2). Substituting Eq. (A4) into Eq. (A2) and using $D_{\mathrm{n}}=\varepsilon_{0}\mathbf{s}\cdot\boldsymbol{\varepsilon}\cdot\mathbf{E}$, we obtain the following equation (recall that $\varepsilon_{\mathrm{sh}}=\varepsilon_{0}$):

$$n_{\mathrm{t}}k_{\mathrm{t}}\Phi-cA_{\parallel}\mathbf{k}_{\mathrm{t}}\cdot\mathbf{b}_{\mathrm{t}}=ik_{\mathrm{t}}^{2}\Delta_{\mathrm{sh}}\mathbf{s}\cdot\boldsymbol{\varepsilon}\cdot\left(\mathbf{n}\Phi-cA_{\parallel}\mathbf{b}\right). \tag{A12}$$

Clearly, if $A_{\parallel}$ is neglected, Eq. (A12) reduces to the SPW dispersion relation for the ES case shown in Ref. [37].

The last step in the derivation is to eliminate Φ (or $A_{\parallel}$) using either Eq. (A10) or (A11), which will then turn Eq. (A12) into an explicit scalar condition to be solved simultaneously with the dispersion relation. First, substituting Eq. (A1) into Eq. (A11), we

obtain

$$\Phi = \frac{cn_{\parallel} A_{\parallel}}{\varepsilon_{\perp}}. \tag{A13}$$

Consequently, substituting Eq. (A13) into Eq. (A12) and using the approximation that $\mathbf{s}\cdot\boldsymbol{\varepsilon} \approx \mathbf{s}\cdot\mathbf{bb}\varepsilon_{\parallel} = b_{\mathrm{n}}\varepsilon_{\parallel}\mathbf{b}$, the desired expression is given by

$$n_{\mathrm{t}}^2 k_{\parallel} - \varepsilon_{\perp}\mathbf{k}_{\mathrm{t}}\cdot\mathbf{b}_{\mathrm{t}} = ik_{\mathrm{t}}^2\Delta_{\mathrm{sh}} b_{\mathrm{n}}\varepsilon_{\parallel}\left(n_{\parallel}^2 - \varepsilon_{\perp}\right). \tag{A14}$$

It is easily verified that Eq. (A14) reduces to the expression for the ES limit when the terms involving an explicit $\varepsilon_{\perp}$ are dropped.

References

[1] J.-M. Noterdaeme and G. Van Oost, Plasma Phys. Control. Fusion **35**, 1481 (1993).

[2] J. R. Myra, D. A. D'Ippolito, D. A. Russell, L. A. Berry, E. F. Jaeger, and M. D. Carter, Nucl. Fusion **46**, S455 (2006).

[3] J. R. Myra, D. A. D'Ippolito, and M. J. Gerver, Nucl. Fusion **30**, 845 (1990).

[4] F. W. Perkins, Nucl. Fusion **29**, 583 (1989).

[5] R. Van Nieuwenhove and G. Van Oost, J. Nucl. Mater. **162-164**, 288 (1989).

[6] R. Chodura and J. Neuhauser, *Proc. 16th European Conf. on Controlled Fusion and Plasma Heating*, *Venice* (European Physical Society, Petit-Lancy, Switzerland, 1989) Vol. 13B, Part III, p. 1089; R. Chodura, Fusion Eng. Des. **12**, 111 (1990).

[7] M. A. Lieberman, IEEE Trans. Plasma Sci. **16**, 638 (1988).

[8] V. A. Godyak and N. Sternberg, Phys. Rev. A **42**, 2299 (1990).

[9] M. Bureš, J. Jacquinot, K. Lawson, M. Stamp, H. P. Summers, D. A. D'Ippolito, and J. R. Myra, Plasma Phys. Control. Fusion **33**, 937 (1991).

[10] D. A. D'Ippolito, J. R. Myra, M. Bureš, and J. Jacquinot, Plasma Phys. Control. Fusion **33**, 607 (1991).

[11] M. Bureš, J. J. Jacquinot, M. F. Stamp, D. D. R. Summers, D. F. H. Start, T. Wade, D. A. D'Ippolito, and J. R. Myra, Nucl. Fusion **32**, 1139 (1992).

[12] D. A. D'Ippolito and J. R. Myra, Phys. Plasmas **3**, 420 (1996).

[13] R. Van Nieuwenhove and G. Van Oost, Plasma Phys. Control. Fusion **34**, 525 (1992).

[14] D. A. D'Ippolito, J. R. Myra, J. Jacquinot, and M. Bures, Phys. Fluids **B5**, 3603 (1993).

[15] J. R. Myra, D. A. D'Ippolito, and Y. L. Ho, Fusion Eng. Des. **31**, 291 (1996).

[16] J. R. Myra and D. A. D'Ippolito, Phys. Plasmas **3**, 699 (1996).

[17] D. A. D'Ippolito, J. R. Myra, J. H. Rogers, K. W. Hill, J. C. Hosea, R. Majeski, G. Schilling, J. R. Wilson, G. R. Hanson, A. C. England, and J. B. Wilgen, Nucl. Fusion **38**, 1543 (1998).

[18] M. Bécoulet, L. Colas, S. Pécoul, J. Gunn, Ph. Ghendrih, A. Bécoulet, and S. Heuraux, Phys. Plasmas **9**, 2619 (2002).

[19] L. Colas, L. Costanzo, C. Desgranges, S. Brémond, J. Bucalossi, G. Agarici, V. Basiuk, B. Beaumont, A. Bécoulet, and F. Nguyen, Nucl. Fusion **43**, 1 (2003).

[20] R. Majeski, P. H. Probert, T. Tanaka, D. Diebold, R. Breun, M. Doczy, R. Fonck, N. Hershkowitz, T. Intrator, G. McKee, P. Nonn, J. Pew, and J. Sorensen, Fusion Eng. Des. **24**, 159 (1994).

[21] J. R. Myra, D. A. D'Ippolito, J. A. Rice, and C. S. Hazelton, J. Nucl. Mater. **249**, 190 (1997).

[22] B. Lipschultz, D. A. Pappas, B. LaBombard, J. E. Rice, D. Smith, and S. J. Wukitch,

Nucl. Fusion **41**, 585 (2001).

[23] S. J. Wukitch, T. Graves, Y. Lin, B. Lipschultz, A. Parisot, M. Reinke, P. T. Bonoli, M. Porkolab, I. H. Hutchinson, E. Marmar, and the Alcator C-Mod Team, *Proc. 21st IAEA Fusion Energy Conf.* (*Chengdu, China, 2006*) (IAEA, Vienna) paper IAEA-CN-149-FT/1-6.

[24] S. J. Wukitch, Y. Lin, B. LaBombard, B. Lipschultz, D. Whyte, and the Alcator C-Mod Team, *Proc. 22nd IAEA Fusion Energy Conf.* (*Geneva, Switzerland, 2008*) (IAEA, Vienna) paper IAEA-CN-165-EX/P6-23.

[25] Vl. V. Bobkov, F. Braun, R. Dux, A. Herrmann, L. Giannone, A. Kallenbach, A. Krivska, H. W. Müller, R. Neu, J.-M. Noterdaeme, T. Pütterich, V. Rohde, J. Schweinzer, A. Sips, I. Zammuto, and ASDEX Upgrade Team, Nucl. Fusion **50**, 035004 (2010).

[26] V. Bobkov, F. Braun, L. Colas, R. Dux, H. Faugel, L. Giannone, A. Herrmann, A. Kallenbach, H. W. Müller, R. Neu, J.-M. Noterdaeme, Th. Pütterich, G. Siegl, E. Wolfrum, and ASDEX Upgrade Team, J. Nucl. Mater. (2010);doi:10.1016/j.jnucmat.2010.08.066

[27] L. Colas, V. Basiuk, B. Beaumont, A. Bécoulet, G. Bosia, S. Brémond, M. Chantant, F. Clairet, A. Ekedahl, E. Faudot, A. Géraud, M. Goniche, S. Heuraux, G. T. Hoang, G. Lombard, L. Millon, R. Mitteau, P. Mollard, K. Vulliez, and the Tore Supra team, Nucl. Fusion **46**, S500 (2006).

[28] L. Colas, A. Ekedahl, M. Goniche, J. P. Gunn, B. Nold, Y. Corre, V. Bobkov, R. Dux, F.

Braun, J.-M. Noterdaeme, M.-L. Mayoral, K. Kirov, J. Mailloux, S. Heuraux, E. Faudot, J. Ongena, ASDEX Upgrade Team, and JET-EFDA contributors, Plasma Phys. Control. Fusion **49**, B35 (2007).

[29] L. Colas, J. P. Gunn, I. Nanobashvili, V. Petržílka, M. Goniche, A. Ekedahl, S. Heuraux, E. Joffrin, F. Saint-Laurent, C. Balorin, C. Lowry, and V. Basiuk, J. Nucl. Mater. **363-365**, 555 (2007).

[30] P. Jacquet, L. Colas, M.-L. Mayoral, G. Arnoux, V. Bobkov, M. Brix, P. Coad, A. Czarnecka, D. Dodt, F. Durodie, A. Ekedahl, D. Frigione, M. Fursdon, E. Gauthier, M. Goniche, M. Graham, E. Joffrin, A. Korotkov, E. Lerche, J. Mailloux, I. Monakhov, C. Noble, J. Ongena, V. Petrzilka, C. Portafaix, F. Rimini, A. Sirinelli, V. Riccardo, Z. Vizvary, A. Widdowson, K.-D. Zastrow, and JET EFDA Contributors, Nucl. Fusion **51**, 103018 (2011).

[31] T. Hellsten and M. Laxåback, Phys. Plasmas **12**, 032505 (2005).

[32] J. R. Myra, D. A. D'Ippolito, and M. Bures, Phys. Plasmas **1**, 2890 (1994).

[33] D. A. D'Ippolito, J. R. Myra, E. F. Jaeger, and L. A. Berry, Phys. Plasmas **15**, 102501 (2008).

[34] D. A. D'Ippolito and J. R. Myra, Phys. Plasmas **13**, 102508 (2006).

[35] E. F. Jaeger, L. A. Berry, J. S. Tolliver, and D. B. Batchelor, Phys. Plasmas **2**, 2597 (1995).

[36] M. D. Carter, P. M. Ryan, D. Hoffman, W. S. Lee, D. Buchberger, and V. Godyak, J. Appl. Phys. **100**, 073305 (2006).

[37] H. Kohno, J. R. Myra, and D. A. D'Ippolito, Phys. Plasmas **19**, 012508 (2012).

[38] H. Kohno, J. R. Myra, and D. A. D'Ippolito, Comput. Phys. Commun. **183**, 2116 (2012).

[39] J. R. Myra and D. A. D'Ippolito, Phys. Rev. Lett.**101**, 195004 (2008).

[40] D. A. D'Ippolito and J. R. Myra, Phys. Plasmas **16**, 022506 (2009).

[41] J. R. Myra and D. A. D'Ippolito, Plasma Phys. Control. Fusion **52**, 015003 (2010).

[42] D. A. D'Ippolito and J. R. Myra, Phys. Plasmas **17**, 072508 (2010).

[43] G. Bekefi, *Radiation Processes in Plasmas*, Wiley (1966).

[44] J. R. Myra, D. A. D'Ippolito, D. W. Forslund, and J. U. Brackbill, Phys. Rev. Lett. **66**, 1173 (1991).

[45] K. Takayama, H. Ikegami, and S. Miyazaki, Phys. Rev. Lett. **5**, 238 (1960).

[46] R. L. Stenzel, Phys. Rev. Lett. **60**, 704 (1988).

[47] R. Ochoukov, D. G. Whyte, D. Brunner, I. Cziegler, B. LaBombard, B. Lipschultz, J. Myra, J. Terry, and S. Wukitch, to be published in J. Nucl. Mater. (2013); http://dx.doi.org/10.1016/j.jnucmat.2013.01.189.

[48] D. A. D'Ippolito, J. R. Myra, R. Ochoukov, and D. G. Whyte, Plasma Phys. Control. Fusion **55**, 085001 (2013).

[49] T. H. Stix, *Waves in Plasmas*, American Institute of Physics (1992).

[50] C. D. Child, Phys. Rev. (Series I) **32**, 492 (1911).

[51] I. Langmuir, Phys. Rev. **21**, 419 (1923).

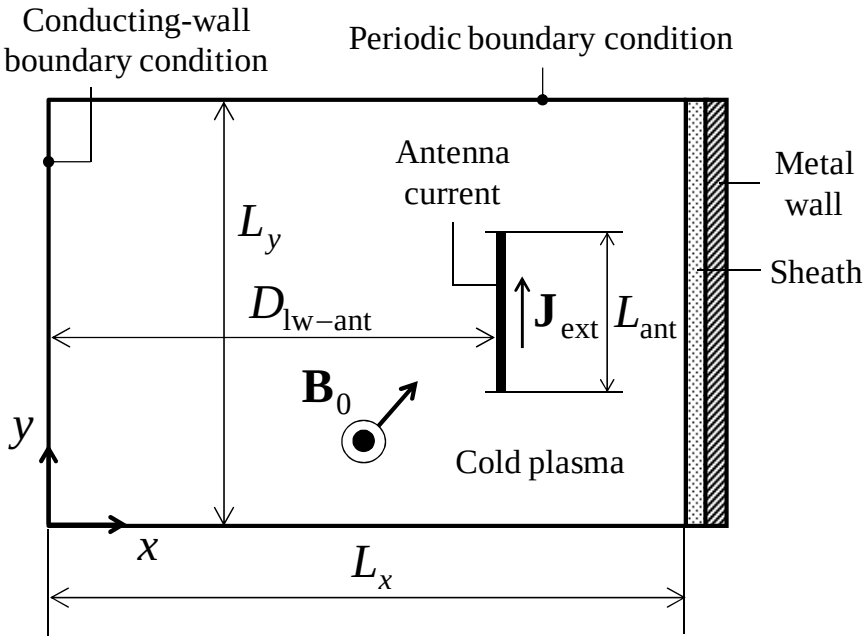

FIG. 1. Singly-periodic slab model to analyze RF sheath-plasma interactions. The x and y directions heuristically correspond to the radial and poloidal directions in a tokamak; however, the geometry is simple and mainly intended to illustrate conceptual points of sheath tangency interactions.

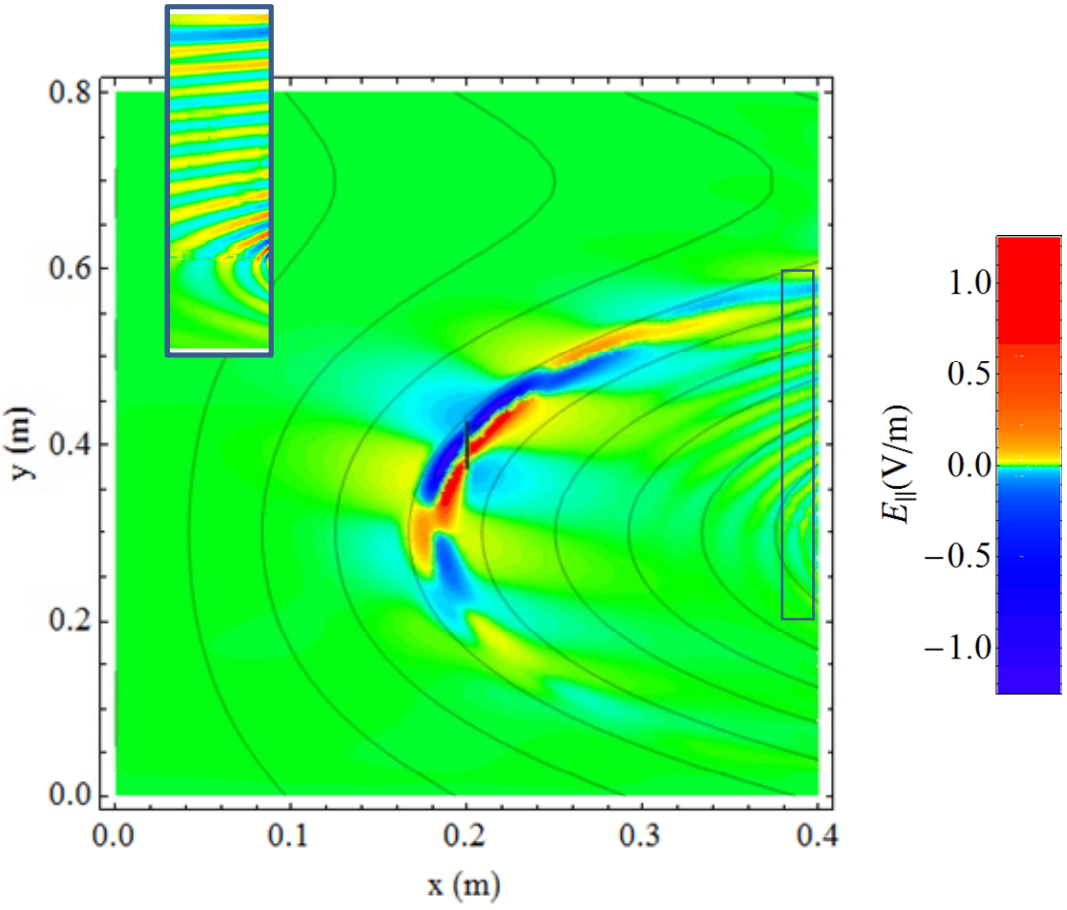

FIG. 2. (Color online) Filled contour plot of $\sinh^{-1}\left[\alpha_{\text{amp}}\,\text{Re}\left(E_{\|}\right)\right]$. Here, $\alpha_{\text{amp}}=1000$. Note that the field from the antenna decays both across and along the field lines, but the decay along background magnetic field is weaker so most of the electric field from the antenna strikes the wall sheath near $y=0.55\,\text{m}$. The boxed region (center right) is shown in an expanded (and spatially distorted) view in the inset to better illustrate the increase in amplitude near the tangency point.

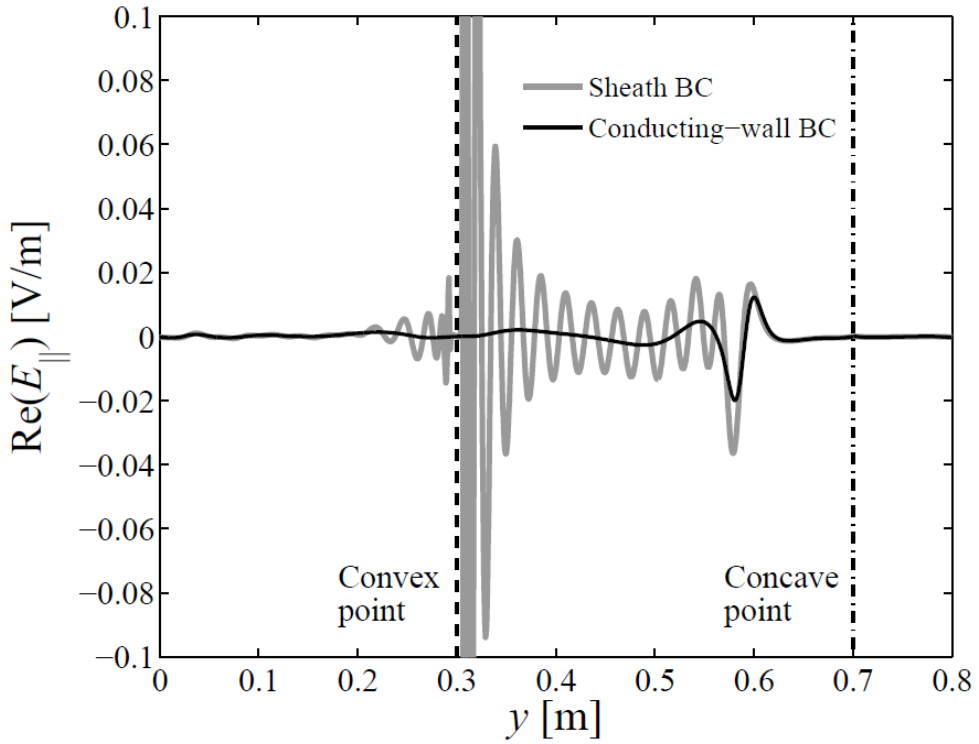

FIG. 3. Plot of the real part of the parallel electric field component along the sheath surface with a comparison to the result for the conducting-wall BC. The vertical dashed and chained lines show the convex and concave points of the magnetic field lines, respectively.

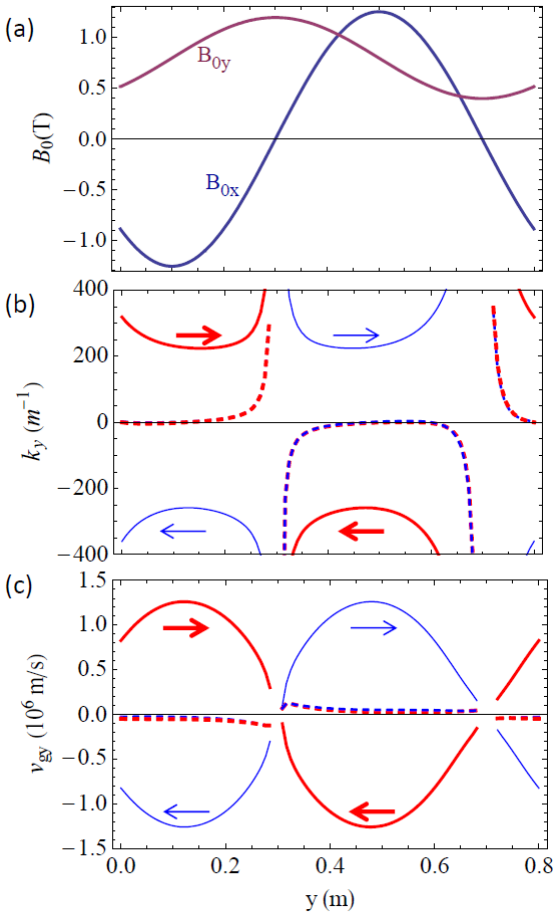

FIG. 4. (Color online) Physical quantities along the sheath surface, which are taken into account in the analytical investigation of the SPW: (a) profiles of the background magnetic field components showing the location of tangency points (where $B_{0x}=0$); (b) plot of the real and imaginary parts of the wavenumber component k_y; and (c) plot of the real and imaginary parts of the group velocity component v_{gy}. In the plots of (b) and (c), the solid and dashed lines denote the real and imaginary parts of the quantities, respectively. Notice the two different modes (i.e., the red, thick mode towards the convex point and the blue, thin mode towards the concave point).

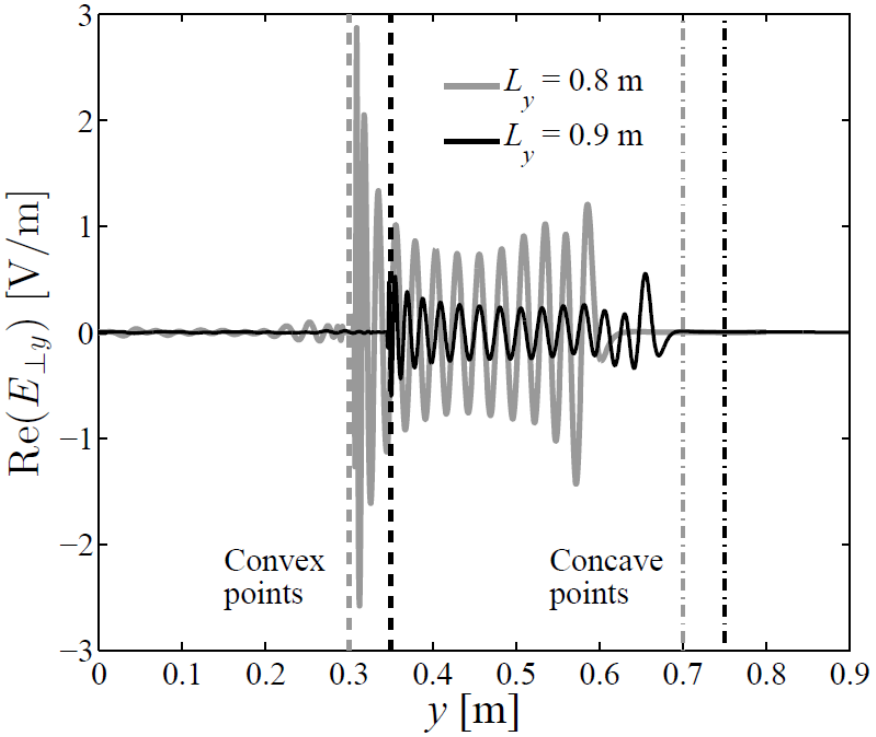

FIG. 5. Comparison of the real part of a perpendicular electric field component, $\mathrm{Re}(E_{\perp y})$, along the sheath surface between the two different periodic lengths in y. The vertical gray dashed and chained lines, respectively, show the convex and concave points of the magnetic field lines for $L_y = 0.8\,\mathrm{m}$, and the vertical black dashed and chained lines correspond to those for $L_y = 0.9\,\mathrm{m}$.

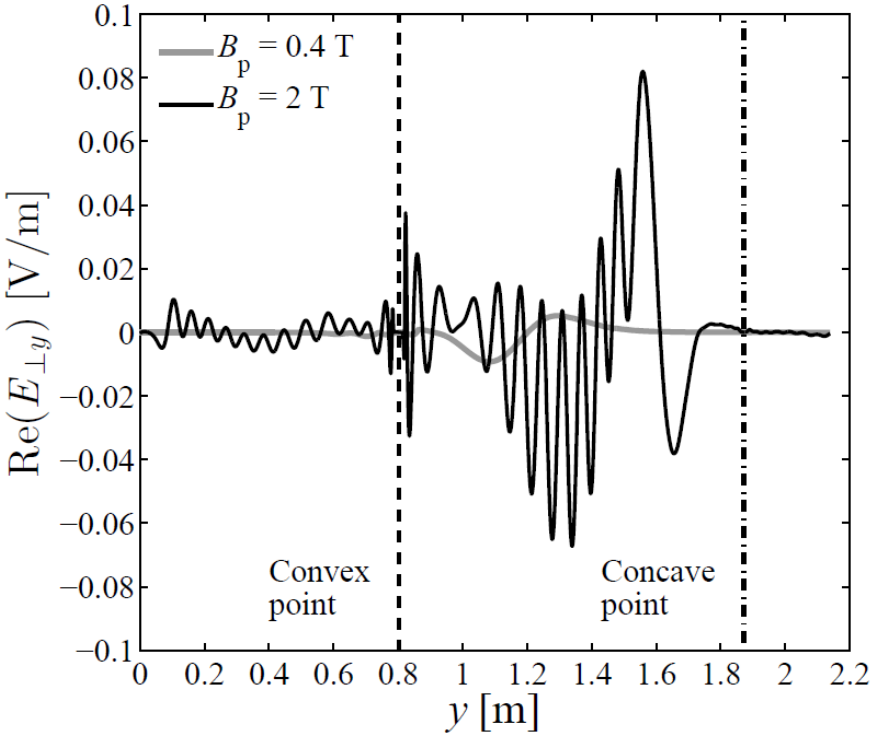

FIG. 6. Comparison of the real part of a perpendicular electric field component, $\mathrm{Re}(E_{\perp y})$, along the sheath surface between the two different poloidal magnetic field strengths. The vertical dashed and chained lines show the convex and concave points of the magnetic field lines, respectively.

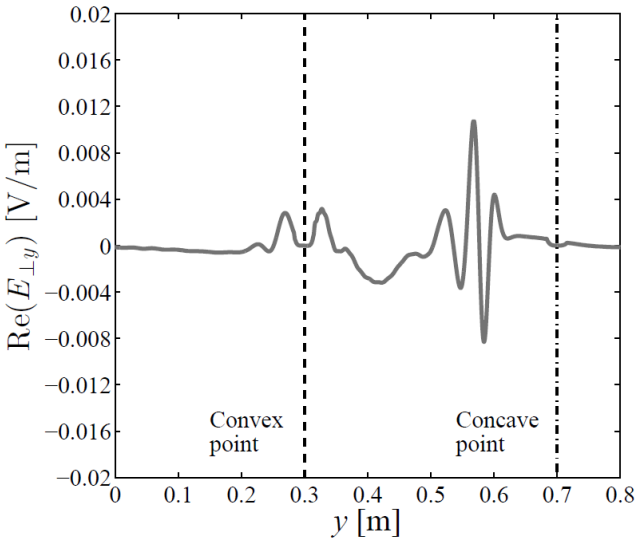

(a)

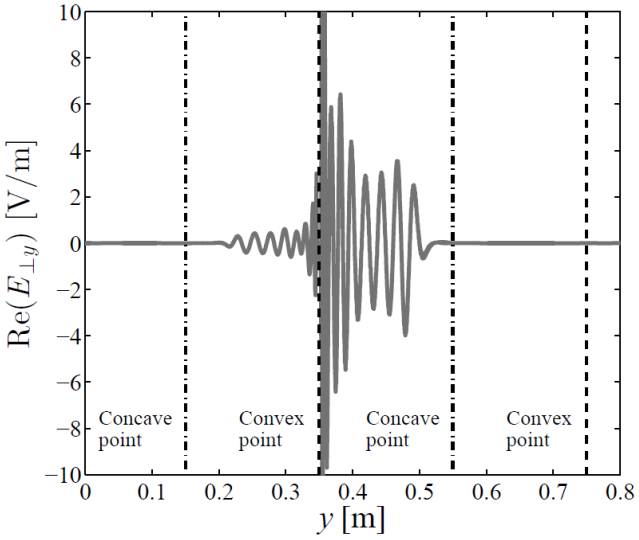

(b)

FIG. 7. Comparison of the real part of a perpendicular electric field component, $\mathrm{Re}(E_{\perp y})$, along the sheath surface for $k_\mathrm{p} = 2\pi/L_y$ (a) and $k_\mathrm{p} = 4\pi/L_y$ (b). The vertical dashed and chained lines show the convex and concave points of the magnetic field lines, respectively.

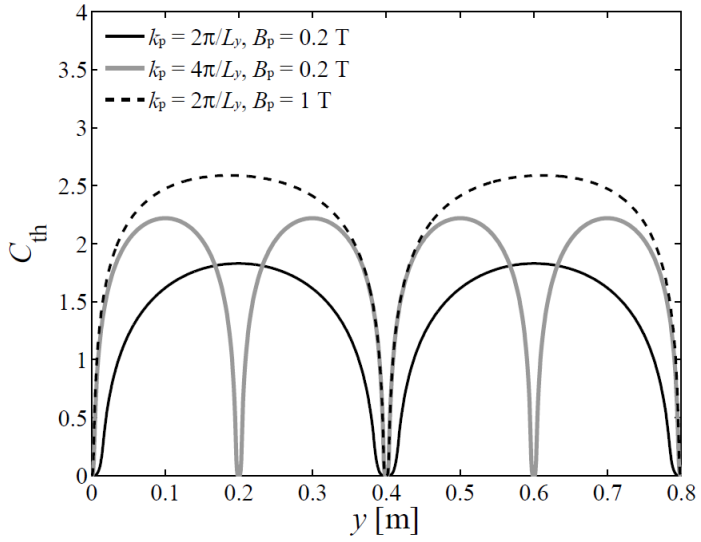

(a)

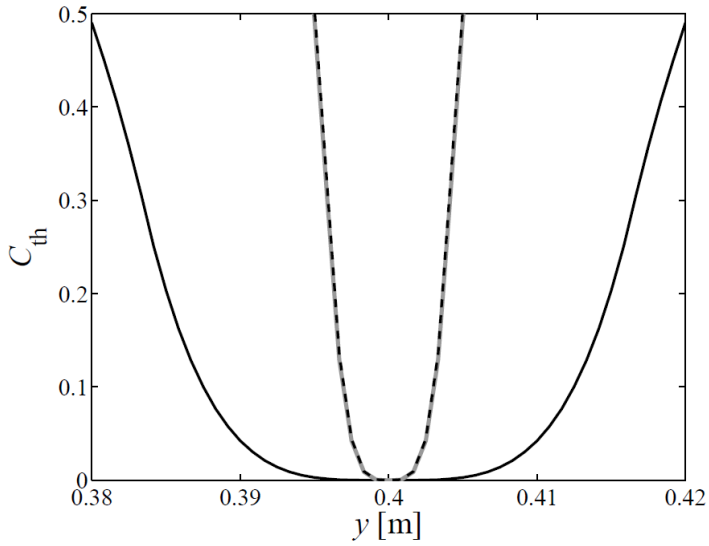

(b)

FIG. 8. (a) Plot of C_{th} for three different choices of k_p and B_p; this graph is magnified in (b) around $y = 0.4\,\mathrm{m}$. Note the rapid variation of C_{th}, and therefore the sheath BC, near the magnetic field tangency points.

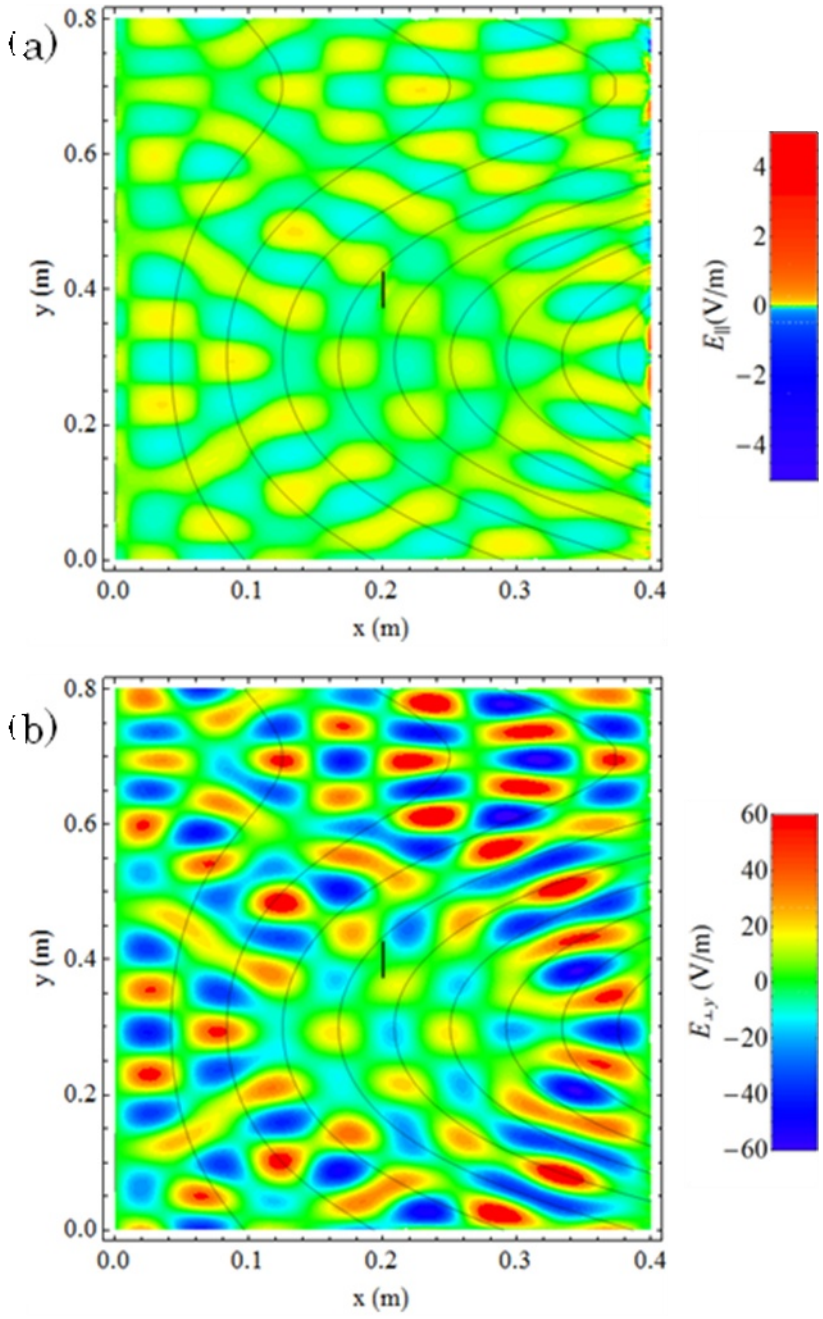

FIG. 9. (Color online) Filled contour plot of $\sinh^{-1}\left[\alpha_{\text{amp}}\,\text{Re}\left(E_{\|}\right)\right]$ (a) and $\sinh^{-1}\left[\alpha_{\text{amp}}\,\text{Re}\left(E_{\perp y}\right)\right]$ (b) for the case described in Sec. III B. Here, the values of α_{amp} are 1000 and 0.1 for $E_{||}$ and $E_{\perp y}$, respectively.

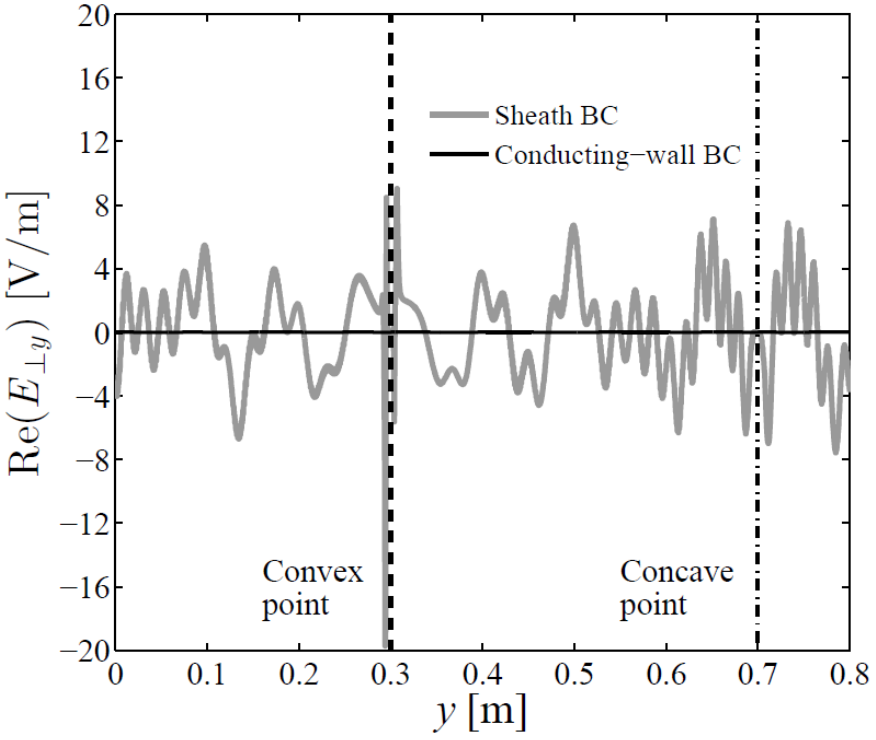

FIG. 10. Plot of the real part of the perpendicular electric field component, $\mathrm{Re}(E_{\perp y})$, along the sheath surface for the case of a propagating FW. The vertical dashed and chained lines show the convex and concave points of the magnetic field lines, respectively. Note the coupling to a small-wavelength mode when the sheath BC is used; the mode disappears when the conducting-wall BC is used.